doi: 10.11144/Javeriana.iyu21-2.ndvs

Non-Invasive Detection of Vortex Street Cavitation[1]

Detección no invasiva de la cavitación en calles de vórtices[2]

Adriana Castro[3]
Francisco Botero[4]

How to cite this article:
A. Castro and F. Botero, "Non-invasive detection of vortex street cavitation," *Ing. Univ.*, vol. 21, no. 2, pp. 155-176, 2017. http://dx.doi.org/10.11144/Javeriana.iyu21-2.ndvs

[1] Submitted on: December 12th, 2016. Accepted on: April 21th, 2017. Scientific and technological research article. This article proceeds from a magister thesis in engineering, Universidad EAFIT, Colombia.
[2] Fecha de recepción: 12 de diciembre de 2016. Fecha de aceptación: 21 de abril de 2017. Artículo de investigación científica y tecnológica. Este artículo se deriva de una tesis de la Maestría en Ingeniería de la Universidad EAFIT, Colombia.
[3] Ingeniera de Producción. MSc. en Ingeniería, Applied Mechanics Research Group, Universidad EAFIT, Medellín, Colombia. E-mail: acastro1@eafit.edu.co
[4] Ingeniero mecánico. Doctor en Ingeniería, Applied Mechanics Research Group, Universidad EAFIT, Medellín, Colombia. E-mail: fboteroh@eafit.edu.co

Abstract

Objective: This paper introduces a methodology for the non-intrusive detection of von Kármán vortex street cavitation. It is based on the cyclostationary analysis of the airborne noise radiated by the collapsing bubbles. *Materials and methods:* A hydrodynamic profile is mounted in the test section of a high-speed cavitation tunnel, and the phenomenon is reproduced under controlled conditions of flow and pressure. The angle of incidence is kept constant. Flow velocity is varied to regulate the vortex generation frequency, and the pressure is adjusted to control the cavitation onset. High-speed photography is used to confirm the occurrence of cavitation in the core of the vortices. A laser vibrometer pointing to the upper surface of the profile validates the fluid-structure interaction due to the vortex shedding. A microphone is used to sense the sound produced by the phenomenon and transmitted to the environment. *Results and discussion:* The cyclic coherence showed uncoupled evidence of the periodic detachment of vortices and the presence or absence of cavitation in their cores, reaching values close to 0.7 for specific frequencies. *Conclusion:* A non-intrusive monitoring approach and a statistical indicator were implemented to allow the diagnosis of such phenomena.

Keywords

non-intrusive monitoring; vortex street cavitation; von Kármán vortex shedding; cyclostationary analysis

Resumen

Objetivo: Este artículo presenta una metodología para la detección no invasiva de calles de vórtices de von Kármán cavitantes. Esta se basa en el análisis cicloestacionario del ruido que produce el colapso de las burbujas. *Materiales y métodos:* Se montó un perfil hidrodinámico en la sección de prueba de un túnel de cavitación de alta velocidad y se reprodujo el fenómeno bajo condiciones controladas de flujo y presión. El ángulo de incidencia se mantuvo constante. Con la velocidad del flujo se regula la frecuencia de generación de vórtices; mientras que con la presión se controla la aparición de cavitación. Se utilizó fotografía de alta velocidad para confirmar la aparición de la cavitación en el núcleo de los vórtices. Un vibrómetro láser que apuntaba a la superficie superior del perfil valida la interacción fluido-estructura debida al desprendimiento de vórtices. Se usó un micrófono para registrar el sonido producido por el fenómeno y que se transmite al ambiente. *Resultados y discusión:* La coherencia cíclica mostró evidencia desacoplada del desprendimiento periódico de vórtices y de la presencia o ausencia de cavitación en sus núcleos, por lo que alcanzó valores cercanos a 0,7 para frecuencias específicas. *Conclusión:* Se implementó un enfoque de monitoreo no invasivo y un indicador estadístico que permiten el diagnóstico de tales fenómenos.

Palabras clave

monitoreo no invasivo; cavitación en calles de vórtices; vórtices de von Kármán; análisis cicloestacionario

Introduction

The formation of a von Kármán vortex street is an amazing hydrodynamic phenomenon: it is like crafting a symphony from chaos. When a bluff body is placed in a fluid turbulent stream, it appears as a well-organized arrangement of vortices that develop harmoniously in the wake at a constant rhythm dictated by the Strouhal number, as shown in Eq. (1). It is defined by the product between the vortex shedding frequency f_s and the inertial time, which in turn is the ratio between the characteristic length L and the reference flow velocity C_{ref} [1]. For a given flow velocity, this is constant, and therein lies both its beauty and danger. Spectacular images involving von Kármán streets can be found from small scales (a few millimeters) [2] to planetary scales (several hundred kilometers) [3], [4]. Nonetheless, the phenomenon becomes undesirable in many technical situations. For instance, the flow within turbomachines is not immune to this phenomenon when fluids flow around parts that behave as truncated bodies. Alternate vortices form by the interaction of detaching conducting shear layers to oscillating lift forces on the structure [5]–[9]; in other words, flow-induced vibrations with an excitation frequency depending on the flowrate. Flow-induced vibration and flow structure interaction are topics of active discussion in specialized literature [10]–[20]. It is well known that objects shedding vortices are excited by the fluctuation of the involved hydrodynamic forces.

$$St_L = \frac{f_s L}{C_{ref}} \tag{1}$$

Resonance may occur if the vortex shedding frequency coincides with a natural frequency of the part or structure. Additionally, when the amplitude of the vibration is large enough, the structural displacement governs the excitation of the fluid, resulting in the phenomenon known as "lock-in." Hence, the vortex shedding frequency locks at the natural frequency of the structure

within a significant range of the flow velocity [21]. Thus, structural displacement accentuates the vorticity of shed vortices to the extent that vortex-induced vibrations might be considered the primary root cause of the premature damage mechanism. In this situation, wearing accelerates, and fatigue becomes the consequence [22], [23].

An example is a guide vane in a Francis turbine. This component serves to regulate the flowrate in order to follow the power demand. Then, at a given power production level, the flow conditions might produce vortices that couple with a natural frequency of the machine. If that occurs, a terrible scenario may ensue; the vane will detach due to fatigue and thus reach the runner, where the structural damage magnifies, leading to incalculable economic losses. This case is sufficient reason for detecting interactions between Kármán vortices and certain sensitive parts before a catastrophic episode occurs. Similar cases can be found in the literature. Authors, such as Egusquiza et al. [24]–[26], recognized lock-in regimes as responsible for the increased vibration and fatigue cracking in hydraulic turbine parts.

Additionally, depending on the fluid kinetic energy and the difference between its absolute pressure and the vapor pressure, cavitation can develop in the core of the vortices. Cavitation, considered by Čudina [27] as the Achilles heel of hydraulic turbomachines, can make the situation worse. Other effects, such as pitting, erosion, and performance degradation, can amend the dynamic generation of vortices [28], compromise design operation ranges, and expose not only the safe operation of a machine but also an operator's safety. In fact, while investigating the flow around a wedge, Young and Holl [29] observed that cavitation alters the vortex shedding frequency up to 25% and has a direct effect on the von Kármán street. Subsequently, Ausoni [21] showed that cavitation can alter the generating frequency up to 15% for a truncated hydrofoil similar to the ones used in turbomachinery.

The implosion of a cavitation bubble produces shock waves that propagate through the fluid, transmit to the machine structure, and eventually radiate airborne waves. In regard to the collapse of a cluster of bubbles instead of a single bubble, broadband noise is produced. If such a phenomenon occurs in travelling Kármán vortices, the signals that can be recorded with a microphone hide information related to the periodicity of the vortex street as well as the randomness induced by cavitation. These inherent properties can be exploited for detection issues with significant operational advantages in productive machinery, such as the non-system interruption required during any stage of the detection process.

In this paper, we present a methodology that allows for the detection of not only the vortex street occurrence but also the formation of cavitation in their cores. The method discussed provides a non-intrusive alternative for conventional methods such as the power spectral density that often fails, decoupling these phenomena. Our experimental study proves that this method can be considered an exceptional solution for monitoring hydraulic turbomachinery because early detection and diagnosis of this phenomenon certainly helps to redefine safe operating ranges, prevents severe damage, and adjusts design guidelines that remain an active topic of research [30]. Moreover, this methodology may be extended to detect similar hydrodynamic phenomena affecting hydraulic turbomachines, such as rotating-cavitation [31], [32]. Validation is performed in a high-speed cavitation tunnel [33]. To this end, a fundamental case study was prepared.

1. Materials and methods

1.1. Airborne noise model

The periodic collapse of bubbles traveling in the cores of vortex streets generates modulating waves that are born in the water and then propagate through the structure and the surrounding air. While the airborne noise emitted by underlying Kármán vortex streets can be considered periodic in nature, the collapse of clouds of bubbles in their cores is rather stochastic. When both processes coincide, the result is quite particular: wide band noise rises and falls in amplitude with a hidden periodicity that obeys a constant Strouhal number, i.e., a so-called Wide Band Modulation (WBM) process. A simplified model for a WBM signal is given in Eq. (2). It is formulated as the product of a sinusoidal wave by additive white Gaussian noise:

$$x(t) = [1 + \sin(2\pi f_s t)]n(t) \tag{2}$$

where $\sin(2\pi f_s t)$ represents the fluctuation associated with the vortices shed at the frequency f_s, while $n(t)$ is the broadband noise due to the cavitation implosion, which not only modulates but also increases, thereby adding to the sinusoidal function. Unit amplitude is assigned to ease interpretation. Based on the modulation property of the Fourier transform, it can be derived that f_s remains hidden when a conventional spectral analysis is performed because the discrete peak of the sine wave becomes invisible after convolution against the white noise in the frequency domain. It is known that Gaussian white noise signals have a perfectly flat power spectrum; thus, the result of the convolution is also flat.

1.2. Signal processing

Although it is well-known that Kármán vortex streets are periodic in nature and that cavitation noise spreads on a wide frequency range, conventional spectral analysis results are, in practice, insufficient to detect them, especially if they are coupled. In addition, the energy content related to such phenomena is often so weak that the sound produced by bubble collapses is ultimately obscured by the background noise. However, since the signals are synchronously phased, the cyclic spectral analysis illustrated by Antoni [34] arises as an exceptional method to uncover diagnostic evidence hidden in the airborne noise signals.

The cyclic power spectrum is the correlation between two spectral components of a signal separated by a given frequency shift ($\alpha \neq 0$), commonly referred to as a cyclic frequency. Then, in order to overcome a relative measure of cyclic coherence between the correlated components, the resulting coefficients are normalized by the power of the signal. Thus, their values conveniently range between 0 and 1, where 0 means no cyclic coherence at all, and 1 means that the components are totally coherent. As modulated signals are observed as sidebands around the carrier frequency [35], they are supposed to be cyclically coherent, i.e., they are separated by a fixed frequency shift. Nonetheless, the case under discussion is special since one of the involved signals is rather random in nature. This inherent particularity of the phenomenon, instead of being a limitation, is a characteristic that can be exploited for diagnostic purposes. It provides wider frequency ranges to investigate.

In fact, Kármán vortices shed at rates no higher than a few hundred per second, which falls into the frequency span of the natural frequencies expected for conventional hydraulic turbomachines. Cavitation shock waves, on the other hand, produce spectral energy spreads of up to several thousand hertz. This important feature allows for isolating spectral regions free of interference coming from other sources of noise (mechanical, structural, hydrodynamic, etc.). Therefore, it is postulated that if f_s in the airborne sound is found to be cyclically coherent at sufficiently high frequencies (several thousand hertz), then that is a strong indication of vortex street cavitation. Conversely, if f_s is found to be cyclically coherent only at lower frequencies (a few hundred hertz), this indicates vortex streets without bubbles imploding in their cores.

In brief, cyclic coherence can be interpreted as a relative measure of the modulation of two components capable of revealing the presence of cavitation in the core of the vortices. Specifically, it appears as a rising component at the

vortex shedding frequency f_s in the frequency domain α. A practical estimator can be obtained from the averaged cyclic coherence, as shown in Eq. (3).

$$\left|\hat{\gamma}_x^{(N)}\left(f;\alpha\right)\right|^2 = \frac{\left|\hat{S}_x^{(N)}\left(f;\alpha\right)\right|^2}{\left|\hat{S}_x^{(N)}\left(f+\frac{\alpha}{2}\right)\right|\left|\hat{S}_x^{(N)}\left(f+\frac{\alpha}{2}\right)\right|} \tag{3}$$

Here, $\hat{S}_x^{(N)}\left(f;\alpha\right)$ stands for the averaged cyclic periodogram estimated from a finite-length record of N samples segmented in K stages and collected at the sampling rate of f_s. In practice, α ranges from 0 to $f_s/2$ according to the Nyquist-Shannon theorem [36], [37]. An estimator of the cyclic periodogram, considering segments of length N_w found in Eq. (4). $X_{Nw}^{(k)}$, is the discrete Fourier transform of the k^{th} windowed stage, and $//w//$ is its Root Mean Square (RMS) value.

$$\hat{S}_x^{(N)}\left(f;\alpha\right) = \frac{1}{KF_S\left\|w\right\|^2}\sum_{K=0}^{K-1} X_{N_w}^{(k)}\left(f+\frac{\alpha}{2}\right)X_{N_w}^{(k)}\left(f-\frac{\alpha}{2}\right) \tag{4}$$

This indicator embodies a certain advantage, cited by Antoni [38], that makes it suitable for portable diagnostic systems. First of all, it does not demand a key phasor signal; second, the length of the segment is independent of the cyclic frequency domain; and third, it is implemented in a straightforward manner and profits from the low computational cost of the Fast Fourier Transform (FFT) algorithm.

Furthermore, the 2D-coherence data obtained from Eq. (3) can be simplified to a 1D diagnostic indicator if the associated frequencies are known, i.e., vortex shedding and resonant frequencies. One strategy to accomplish this is to scrutinize the cyclic-frequency domain within a band containing the vortex shedding frequency (fundamental, harmonics, and sidebands) while integrating the cyclic coherence along the sampled frequency domain. The integrated cyclic coherence (ICC) presented in Eq. (5) is adopted from [38]. Here, the scrutinized frequency range is delimited by $K_1(\alpha)$ and $K_2(\alpha)$ with $K_1(\alpha) < K_2(\alpha)$, while the frequency domain is bounded by f_k.

$$ICC_x^{(N)}\left(\alpha\right) = \frac{1}{K_2\left(\alpha\right)-K_1\left(\alpha\right)}\sum_{k=K_1(\alpha)}^{K_2(\alpha)} X_{N_w}^{(k)}\left|\hat{\gamma}_x^{(N)}\left(f_k;\alpha\right)\right|^2 \tag{5}$$

The expected result from this diagnostic indicator is a 1D vector that can be conveniently represented as a plot (ICC vs. α). However, in order to uncouple both phenomena, the frequency domain must be split into two parts: The low frequency band is intended to reveal the vortex street, while the higher frequencies are processed to expose the presence of bubbles imploding in the cores of the vortices. In any plot, a prominent peak rising at f_s (and integer multiples) indicates an episode of either vortex street or vortex street cavitation.

1.3. Diagnostic: Hypothesis test

A probabilistic approach is adopted to assist the assessment of both ICC patterns obtained from the measured airborne sound. It is assumed that one pattern carries the signature of Kármán vortex shedding and the other reveals the occurrence of cavitation in the core of the vortices. Therefore, let α be the characteristic cyclic frequency at which a vortex is shed, and let p be the false alarm probability. Then, the two alternatives formulated for a hypothesis test are as follows:

H_0: "Airborne noise signal does not contain diagnostics information at α."
H_1: "Airborne noise signal contains diagnostics information at α."

Subsequently, the decision rule that maximizes the probability of detection for a given probability of false alarm is

"Reject H_0 if Eq. (6) is satisfied."

$$\left|\hat{\gamma}_x^{(N)}\left(f;\alpha\right)\right|^2 = \frac{\left|\hat{S}_x^{(N)}\left(f;\alpha\right)\right|^2}{\hat{S}_x^{(N)}\left(f+\frac{\alpha}{2}\right)\hat{S}_x^{(N)}\left(f+\frac{\alpha}{2}\right)} \geq \frac{\xi}{2}\cdot\chi^2_{1-p,2} \tag{6}$$

The statistical threshold depends on the chi-square value $\chi^2_{1\text{-}p,2}$, for the false alarm probability p (with two degrees of freedom), and the variance reduction factor ξ is defined as:

$$\xi = \sum_{k=-K+1}^{K-1} R_w\left[kR\right]^2 \cdot \frac{K-|k|}{K^2} \tag{7}$$

Where $R_w[n]$ stands for the autocorrelation function of the signal segment $w[n]$. The optimality of this decision rule is proved in [34].

1.4. Case study and experimental setup

A high-speed cavitation tunnel, described in detail by Avellan et al. in [33], is adapted to test a NACA 0009 hydrofoil made of stainless steel. It consists of a hydraulic circuit able to provide up to 50 m/s of free-stream velocity at the input of the test section ($150\times150\times750$ mm^3). Pressure can be adjusted from a vacuum up to 16 bar. The hydrofoil, which is fixed from one side to the test section with an angle of attack of 0°, features a maximum thickness of 10 mm and a truncated trailing edge. Its chord length is $L=100$ mm. Additionally, special care is taken on the roughness of the surface to trip the boundary layer transition from a flow velocity of 5 m/s. Sketches of the cavitation tunnel and hydrofoil geometry are provided in Figure 1. Two parameters are independently manipulated in order to control the behavior of the wake. The flow velocity is adjusted to control the frequency of the Kármán vortices (according to the Strouhal number), and static pressure induces cavitation. It is anticipated that bubbles are more likely to form first in the core of the vortices because of the hydrodynamics of the phenomenon; in other words, the testing parameters can be adjusted to produce cavitation only in the vortex street.

Figure 1. (a) Hydraulic circuit of the high-speed cavitation tunnel. (b) Blunt trailing edge NACA 0009 hydrofoil made of stainless steel

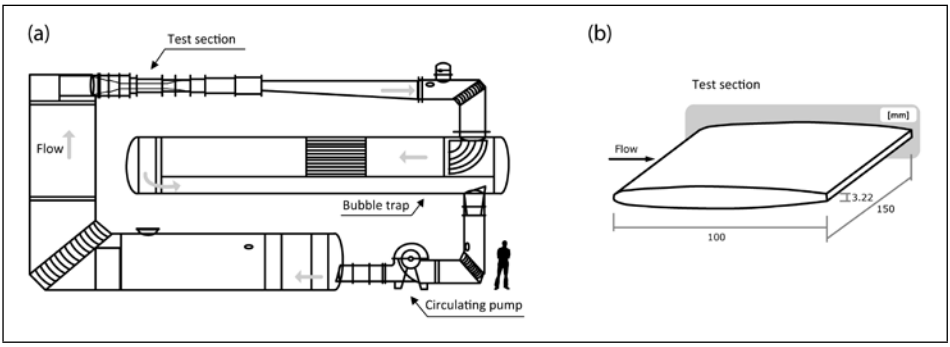

Source: Authors' own creation.

Flow velocity measured at the inlet of the test section (C_{ref}) is purposely set at 16 m/s. It maintains high Reynolds numbers (Re) around the hydrofoil and corresponds, at the same time, to a lock-in condition. High Reynolds numbers ensure a turbulent flow regime required to form turbulent vortex streets [39]. The Reynolds number, as stated in Eq. (8), is calculated considering a character-

istic length L equal to the chord of the hydrofoil. The lock-in condition favors the development of better-organized vortex streets.

$$Re_L = \frac{C_{ref} L}{v} \tag{8}$$

Regarding cavitation, two operating states are defined based on the reference pressure measured in the test section, i.e., vortex streets with and without cavitation. Visual inspection of the wake by means of a high-speed camera is the main criterion to assess the pressure value for each state. An image resolution of 1024×320 pixels at 18000 fps is adequate to detect and analyze the vorticial cavitation structures forming below 1 kHz. Pressure is gradually increased until all cavitation is extinguished. When a steady state is achieved, static pressure at that moment is adopted as the reference pressure, and airborne noise is recorded. Similarly, pressure is slowly decreased until bubbles continuously form only in the wake and vortex street cavitation becomes evident. This state defines the pressure level corresponding to the second operating state. The cavitation number σ, defined in Eq. (9), is used to characterize both of the defined operating states. It is essentially the ratio between the static and dynamic pressures; p_{ref} stands for the static pressure at the test section inlet, p_v represents the vapor pressure and ρ is the density of the fluid.

$$\sigma = \frac{p_{ref} - p_v}{\frac{1}{2}\rho C_{ref}^2} \tag{9}$$

The dynamic response is monitored directly on the hydrofoil surface using a Polytec PDV100 laser vibrometer. This system has a dynamic range from 0 to 20 kHz. The monitoring point is chosen based on the shapes of the first four modal behaviors of the hydrofoil (<2 kHz). To support this, a numeric modal analysis of a finite element model is investigated prior to experimentation. The resulting mode shapes, indicating the selected monitoring point, are arranged in Figure 2. Such a point is located at mid-span and 10% of the chord length from the trailing edge. It is selected based on the response of the hydrofoil. The lighter the surface is, the larger the amplitude response.

Figure 2. Location of the vibration monitoring point as defined from the results of the numerical modal analysis of the hydrofoil

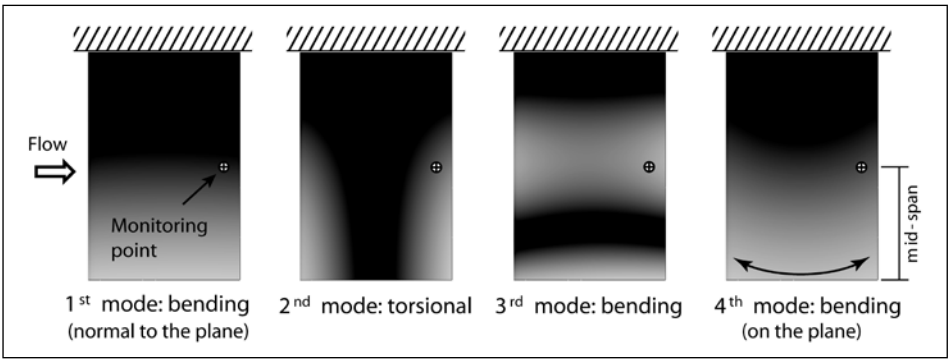

Source: Authors' own creation.

Radiated sound is sensed using a Sennheiser e614 super-cardioid electret condenser microphone. This microphone is selected because it exhibits a wide frequency response (20 to 20000 Hz), an effective rejection of incidental rear noise and fast transient response. The microphone is mounted on a rigid and independent support, aimed at the test section, half a meter away and facing the upper surface of the hydrofoil. Sound and vibration signals are simultaneously sampled at 40000 samples/second and 24-bit resolution using an NI PXI-4472B dynamic signal acquisition module. This module is fitted with analog and real-time digital filters implemented in the hardware to prevent aliasing. Synchronization with the high-speed camera is achieved by means of an external trigger signal.

2. Results and discussion

An overview of the vortex shedding frequencies as a function of flow velocity is shown in Figure 3a. It is derived from the spectral estimation of the vibration measurements using Welch's method [40] and the parameters indicated in Table 1. A linear trend is superimposed to initially highlight the Strouhal ratio and subsequently highlight the lock-in condition on which our experiment focuses (gray-filled markers). It is known that for lock-in, the trailing edge vibration produces more organized wake structures that are easier to visualize. The RMS amplitudes of the hydrofoil vibration and the structure-borne noise for the explored flow velocities are plotted in Figure 3b. Only the shedding frequency-related components are tagged. Surprisingly, vibrations and sounds behave differently. They do not exhibit the maximum peak under the same conditions.

For example, at C_{ref} = 16 m/s, when the first torsion mode is reached, vibration is stronger but sound pressure level is weaker. Nonetheless, the focus is placed on this condition since stronger vibrations ease visualization and dynamic characterization, as evidenced in Figure 4. Mode shapes were verified by performing synchronized vibration measurements at different locations of the hydrofoil surface. Photographs in the figure correspond to the selected operating points. As observed, the wake structure in Picture 4a is not evident. The structure became visible once the σ value decreased and cavitation occurred; changes in the fluid phase made light refract and reflect conveniently. The vortex street is therefore revealed, and the cavitation occurrence is validated, as seen in Figure 4b.

Figure 3. (a) Vortex shedding frequency for different upstream velocities. (b) Airborne noise and vibration of the hydrofoil trailing edge for different upstream velocities

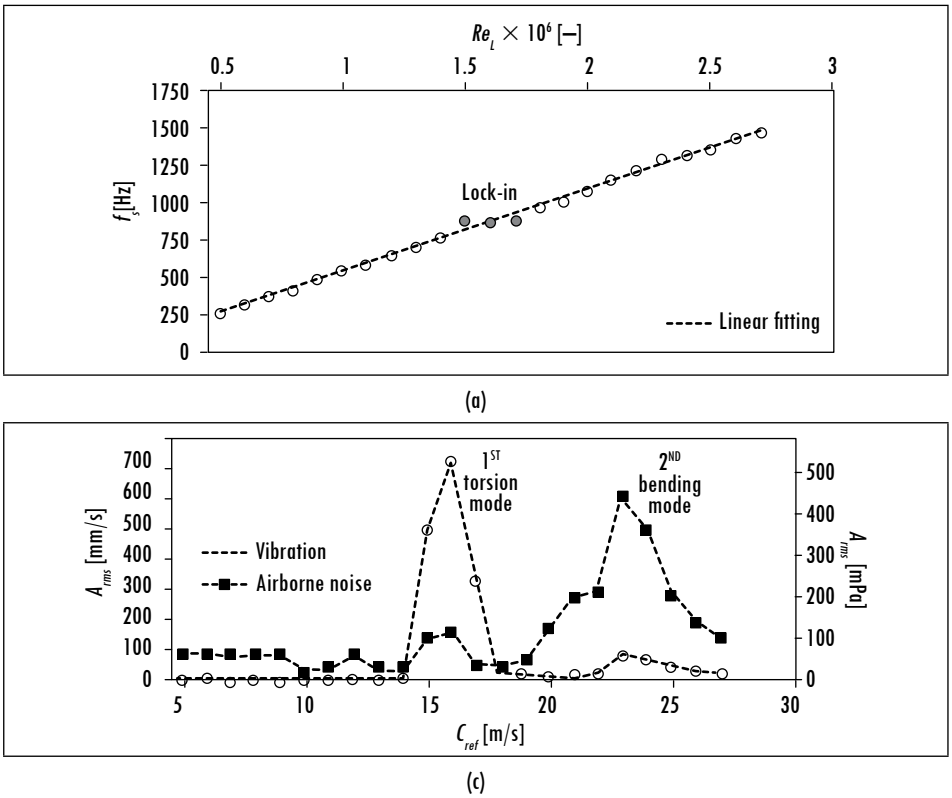

Source: Authors' own creation.

Figure 4. High-speed photographs for (a) high and (b) low cavitation indexes

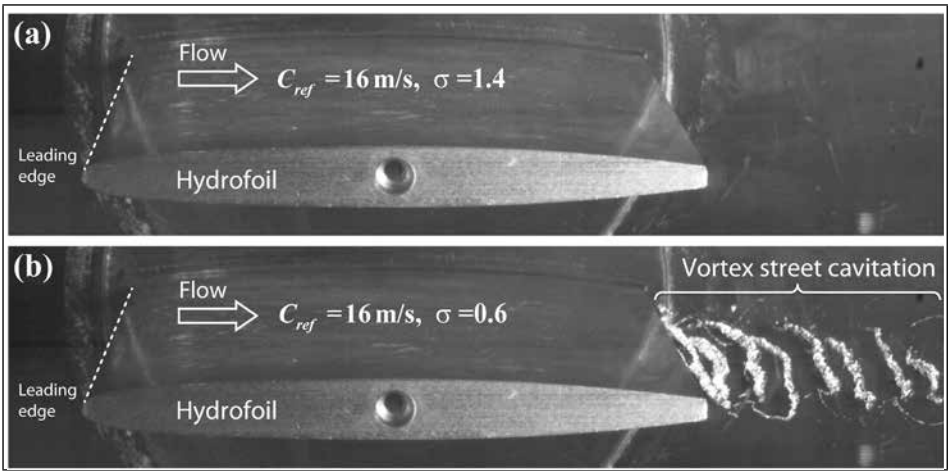

Source: Authors' own creation.

Flow-induced vibrations are almost imperceptible in the high-speed frame sequence, but they can be fully recovered from the vibrations measured from the monitoring point. Such signals, checked against the video, are used to determine the vortex shedding frequency (f_s = 880 Hz) and correlate the synchronized airborne noise. Figure 5 displays the sound pressure signals of the experiment during one second for both operating conditions, i.e., (a) the cavitation-free regime and (b) while undergoing vortex street cavitation. At first glance, both seem moderately stationary. The sound pressure level (SPL) is determined for each case, obtained from Eq. (10) for a reference value of p_{ref} = 20 μPa. The power of the recorded sound increases by about one and a half times when cavitation begins; nonetheless, the reader is advised to keep in mind that this increment is not totally due to bubble collapses. These signals are very susceptible to external noise sources and therefore highly polluted. For instance, a vacuum pump is activated to decrease the sigma value. There exists no case where particular signatures can be associated with the undergoing periodic phenomenon.

$$SPL = 20\log\left(\frac{p_{rms}}{p_{ref}}\right) \tag{10}$$

Figure 5. Airborne noise recorded at (a) high and (b) low cavitation indexes

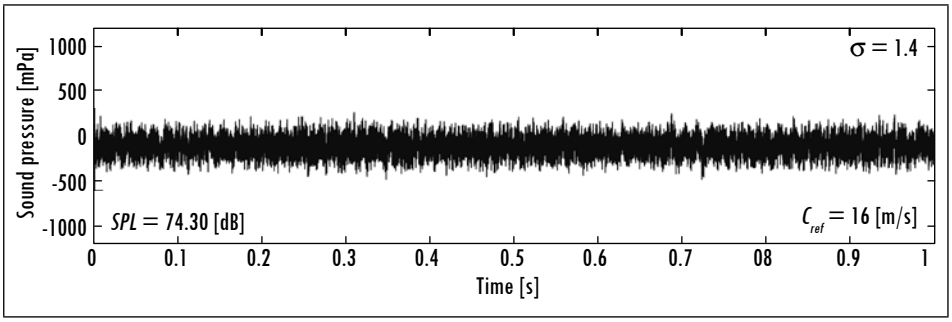

(a) Cavitation-free regime

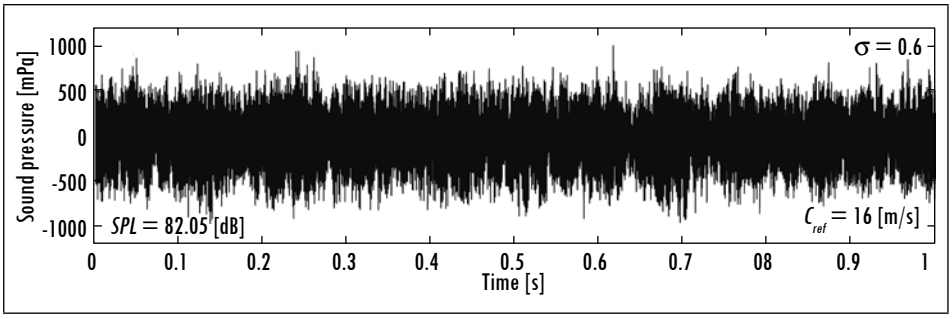

(b) Cavitation-free regime

Source: Authors' own creation.

An insight into the frequency distribution of the airborne noise is intended by means of a power spectral estimation. Welch's method, with parameters listed in Table 1, is used, and results are presented in Figure 6. To facilitate reading, values are plotted under the same amplitude scale, while the frequency domain is limited to 5 kHz. It is observed that the component corresponding to the shedding frequency f_s rises in both cases, confirming the excitation due to the vortex shedding, even when vortices are invisible ($\sigma = 1.4$). The same goes for the harmonics, with a special emphasis on the third harmonic. In particular, the power spectral density in (b) shows significant changes. As predicted by the adopted model in Eq. 2, when the σ value is decreased, the random collapses of cavitation bubbles affect the entire frequency span, burying components related to the shedding vortex. Curiously, the added energy spreads out over the frequency domain almost uniformly, suggesting that the sound pressure level increases, but this does not necessarily provide enough evidence for diagnostic purposes.

Table 1. Welch's method estimation parameters

Sampling frequency (f_s)	40000 Samples/s
Record length (N)	2^{20} Samples
Window type	Hanning
Window length (N_w)	2^{16} Samples
Frequency resolution (Δ_f)	0.61 Hz
Overlap	2/3

Source: Authors' own creation.

Figure 6. Power spectral density of airborne noise at (a) high and (b) low cavitation indexes

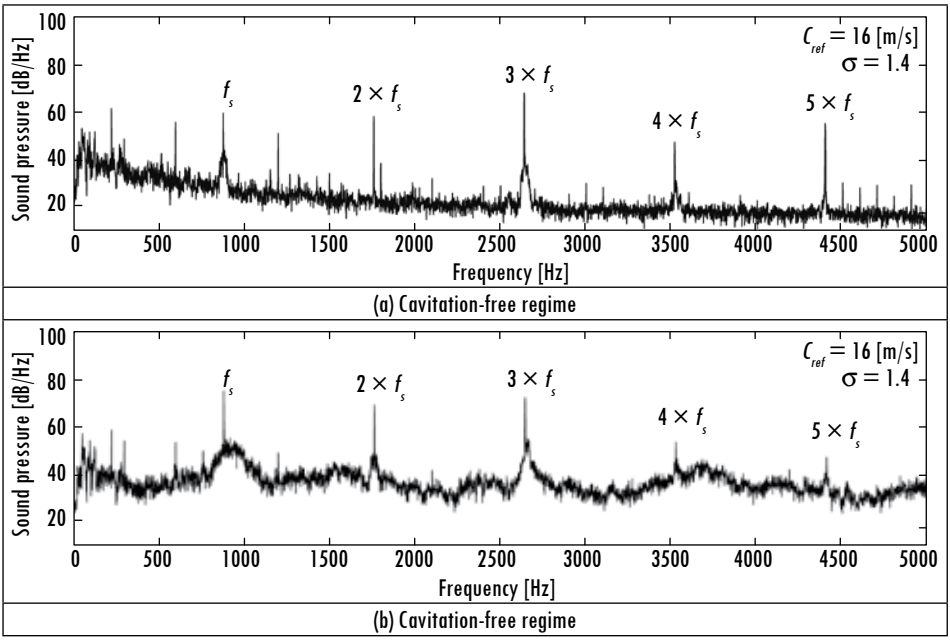

Source: Authors' own creation.

Cyclic coherence was computed for both operating conditions using parameters listed in Table 2 and according to the introduced methodology. Special care was taken when selecting the cyclic frequency resolution to achieve sufficient statistical stability: $\Delta f/\Delta\alpha > 1500$. The results, as a function of the sampled frequency f and cyclic frequency α domains, are shown in Figure 7a and Figure 8a. The scales are the same, and the shedding frequency and multiples are specifically designated. A strong coherence is observed below 10 kHz in the f domain at f_s in

the α domain. This coherence is attributed to the periodic excitation due to the vortex shedding. Amazingly, when cavitation occurs, i.e., σ=0.6, such coherence decreases while a higher and well differentiated band notably ascends. This is undoubtedly the signature of the vortex street cavitation; cavitation bubbles collapsing rhythmically at f_s cause this coupling effect.

Table 2. Cyclic coherence estimation parameters

Record length (N)	2^{20} Samples
Window type	Hanning
Window length (N_w)	2^5 Samples
Overlap	2/3
Frequency resolution (Δ_f)	1250 Hz
Cyclic frequency resolution ($\Delta\alpha$)	1 Hz
Scrutinized cyclic frequency range	$K_1(\alpha) = 500$; $K_2(\alpha) = 2000$

Source: Authors' own creation.

Figure 7. Cyclostationary analysis at high cavitation index

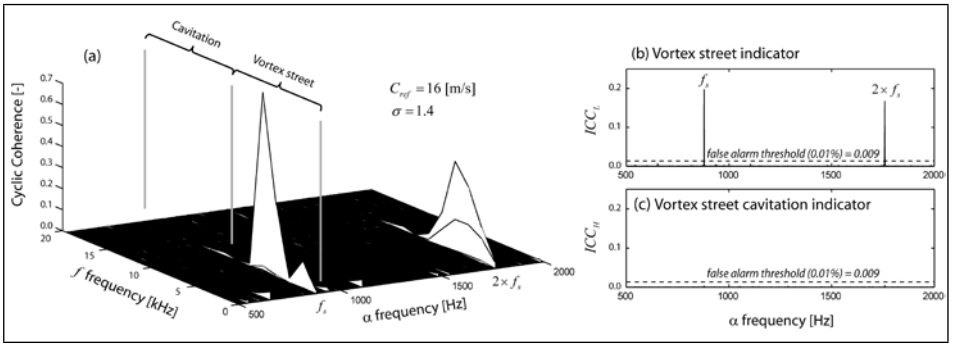

Source: Authors' own creation.

The results above provide a reason to divide the f domain into two halves. It is observed that coherence is stronger from 7 to 10 kHz. An equivalent conclusion can be retrieved from a frequency response test for both vibrations and sounds (room response). Nevertheless, once cavitation enters the stage, part of the coherence strength seems to move and spread to higher frequencies. This is precisely the expected behavior of the energy distribution due to the randomness of bubble collapses, i.e., n(t) in Eq. (2). This is the case for the fundamental frequency and its harmonics. Thus, two independent regions are identified: a low-frequency region from 0 to 10 kHz is attributed to the periodic excitation

of the vortex shedding and a high-frequency region from 10 to 20 kHz is attributed to the cavitation in their cores.

Graphs (b) and (c) in both Figure 7 and Figure 8 correspond to the integration of each of the identified regions. Here, ICC_L represents the integrated cyclic coherence of the low-frequency region, while ICC_H stands for the high-frequency region, i.e., the region associated to cavitation. These indicators substantially simplify the diagnostic assessment procedure and facilitate the establishment of decision rules. For such purposes, the statistical false alarm threshold is calculated for a probability of 0.01% and superimposed on said graphs. The evidence is overwhelming. Only components at frequencies related to the vortex shedding are prominent and well beyond the false alarm limit.

Figure 8. Cyclostationary analysis at low cavitation index

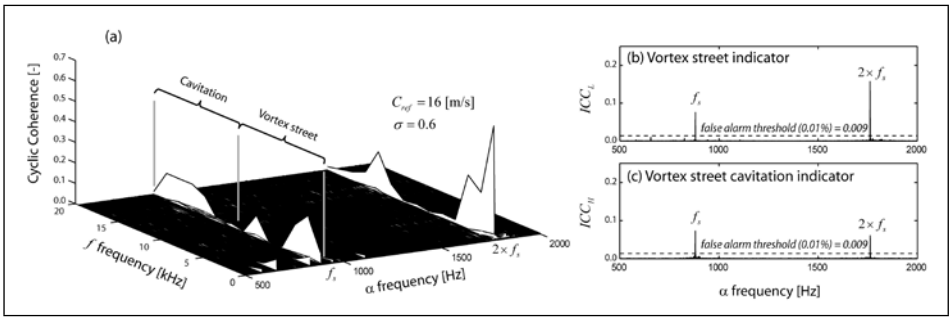

Source: Authors' own creation.

These findings are consistent with the results reported by Farhat et al. in [41], and extended later to further techniques by Escaler et al. in [42] for Francis turbines and Botero et al. in [43], [44] for reversible pump turbines. Indeed, it explains why they started filtering the time domain signals in a wide frequency band of several kilohertz to remove low-frequency content before demodulation procedures (see [35]), which turns out to be a special case of the cyclic coherence. Furthermore, this analysis provides a full panorama of the structured content of the signal, i.e., the cut-off frequency of the filter can be accurately determined and fixed from now on.

3. Discussion and conclusions

The purpose of this paper is to introduce a fully non-intrusive approach to detect vortex street cavitation. It is based on the cyclic spectral analysis of the emitted noise (audible range) and is extendable to the structure-borne noise.

We proved that the symptomatic pattern of the collapsing process of rows of cavities is essentially random and cyclostationary, and thus adequately preserved in the high-frequency range (>10 kHz) of the structural vibrations and even in the radiated airborne noise. In fact, we explain why some demodulating approaches found in the literature empirically use high-pass filters and provide some indications to effectively set its cut-off frequency.

The innovation of this approach lies essentially in its ability to detect the vortex street occurrence and the formation of cavitation in their cores, providing a non-intrusive alternative to conventional techniques, such as the power spectral density that fails in decoupling these phenomena. Thus, its implementation impacts directly on the monitoring of hydraulic turbomachinery and their components because early detection and diagnosis of these phenomena certainly help to redefine safe maneuvering, prevent severe damage, and adjust design guidelines.

Despite the simplicity of the instrumentation and computational background required, the implementation of this approach in practice may encounter some obstacles. For instance, the low sound power of the vortex street cavitation presents two important risks. First, its implementation could become economically unviable due to the need for sophisticated microphones and high-performance acquisition systems. Second, the intensity and bandwidth of the background noise of industrial environments could deform the carrier signal in such a way that recovering the signature of the cavitation would be impractical. Another limitation of the method rises when the coupling between cavitation and vortex streets occurs simultaneously in more than two rotating elements of the same hydraulic system, such as the case of the impeller of a centrifugal pump or the runner of a reaction turbine. These difficulties call for further experimental investigations. The next step is to involve a hostile environment (noise and vibration) and the controlled manifestation of a vortex street cavitation in rotating elements in the same case study.

This new approach is based on a mathematical model based on previous works related to similar phenomena. In short, it consists of integrating the cyclic coherent content of two distinctly scrutinized frequency ranges. Fundamental experiments are carried out in a high cavitation tunnel using specialized state-of-the-art instrumentation in order to find such ranges and therefore validate the model. Basically, a 2D hydrofoil subjected to a specific flow velocity undergoing vortex streets is observed at two different pressures. Pressure is carefully regulated in order to control the inception of vortex street cavitation. The

harmonic nature of vortex shedding is found in the low-frequency range, while the randomness of bubble collapses is detected in the high-frequency range. When reading the integrated cyclic coherence of each of the ranges, a simpler indicator revealing the characteristic signature of each phenomenon is obtained. This result is compared with a statistical limit (optimal statistical test) based on the false-alarm probability.

Acknowledgment

The present investigation was carried out in the framework of Karcavit research project, in a partnership with the Applied Mechanics research group of EAFIT and the Laboratory for hydraulic Machines (LMH) of the EPFL. The authors would like to thank the LMH and EAFIT for their technical and financial support (research projects 538-000038, 342-000031, 435-000044 and 326-000461). A special expression of gratitude is conveyed to the staff of the LMH.

References

[1] P. Ausoni, A. Zobeiri, F. Avellan, and M. Farhat, "The effects of a tripped turbulent boundary layer on vortex shedding from a blunt trailing edge hydrofoil," *J. Fluids Eng.*, vol. 134, no. 5, p. 51207, May 2012.

[2] A. Zobeiri, "Effect of hydrofoil trailing edge geometry on the wake dynamics," Ph.D. dissertation, EPFL, Lausanne, 2012. [Online]. Available: https://infoscience.epfl.ch/record/168992/files/EPFL_TH5218.pdf

[3] K. P. Chopra, "Atmospheric and oceanic flow problems introduced by islands," *Adv. Geophys.*, vol. 16, pp. 297–421, 1973.

[4] NASA, "NASA Earth Observatory: A swirl of clouds over the Pacific," 22-May-2013. [Online]. Available: http://earthobservatory.nasa.gov/IOTD/view.php?id=81883, Accessed on: Jun 19, 2015.

[5] A. Roshko, "On the development of turbulent wakes from vortex streets," CA Inst. Tech, 1954. [Online]. Available: http://authors.library.caltech.edu/428/1/ROSnacarpt1191.pdf

[6] J. H. Gerrard, "The mechanics of the formation region of vortices behind bluff bodies," *J. Fluid Mech.*, vol. 25, no. 2, p. 401, Jun. 1966.

[7] P. W. Bearman, "Vortex shedding from oscillating bluff bodies," *Annu. Rev. Fluid Mech.*, vol. 16, no. 1, pp. 195–222, Jan. 1984.

[8] O. M. Griffin and O. M., "A note on bluff body vortex formation," *J. Fluid Mech.*, vol. 284, no. 1, p. 217, Feb. 1995.

[9] C. H. K. Williamson and A. Roshko, "Vortex formation in the wake of an oscillating cylinder," *J. Fluids Struct.*, vol. 2, no. 4, pp. 355–381, 1988.

[10] C. Trivedi, "A review on fluid structure interaction in hydraulic turbines: A focus on hydrodynamic damping," *Eng. Fail. Anal.*, vol. 77, pp. 1–22, 2017.

[11] D. Ni, M. Yang, N. Zhang, B. Gao, and Z. Li, "Unsteady flow structures and pressure pulsations in a nuclear reactor coolant pump with spherical casing," *J. Fluids Eng.*, vol. 139, no. 5, p. 51103, Mar. 2017.

[12] J. Tian, Z. Zhang, Z. Ni, and H. Hua, "Flow-induced vibration analysis of elastic propellers in a cyclic inflow: An experimental and numerical study," *Phys. Procedia*, vol. 65, pp. 47–59, 2017.

[13] A. Müller, A. Favrel, C. Landry, and F. Avellan, "Fluid–structure interaction mechanisms leading to dangerous power swings in Francis turbines at full load," *J. Fluids Struct.*, vol. 69, pp. 56–71, 2017.

[14] H. Kou, J. Lin, J. Zhang, and X. Fu, "Dynamic and fatigue compressor blade characteristics during fluid- structure interaction: Part I—Blade modelling and vibration analysis," *Eng. Fail. Anal.*, vol. 76, pp. 80–98, 2017.

[15] J. Cisonni, A. D. Lucey, N. S. J. Elliott, and M. Heil, "The stability of a flexible cantilever in viscous channel flow," *J. Sound Vib.*, vol. 396, pp. 186–202, 2017.

[16] W. K. Bonness, J. B. Fahnline, P. D. Lysak, and M. R. Shepherd, "Modal forcing functions for structural vibration from turbulent boundary layer flow," *J. Sound Vib.*, vol. 395, pp. 224–239, 2017.

[17] A. Bauknecht, B. Ewers, O. Schneider, and M. Raffel, "Blade tip vortex measurements on actively twisted rotor blades," *Exp. Fluids*, vol. 58, no. 5, p. 49, May 2017.

[18] Y. Zhao, G. Wang, and B. Huang, "Vortex structure analysis of unsteady cloud cavitating flows around a hydrofoil," *Mod. Phys. Lett. B*, vol. 30, no. 2, p. 1550275, Jan. 2016.

[19] M. J. Thorsen, S. Sævik, and C. M. Larsen, "Fatigue damage from time domain simulation of combined in-line and cross-flow vortex-induced vibrations," *Mar. Struct.*, vol. 41, pp. 200–222, Apr. 2015.

[20] Z. Yao, F. Wang, M. Dreyer, and M. Farhat, "Effect of trailing edge shape on hydrodynamic damping for a hydrofoil," *J. Fluids Struct.*, vol. 51, pp. 189–198, Nov. 2014.

[21] P. Ausoni, M. Farhat, X. Escaler, E. Egusquiza, and F. Avellan, "Cavitation Influence on von Kármán Vortex Shedding and Induced Hydrofoil Vibrations," *J. Fluids Eng.*, vol. 129, no. 8, p. 966, Aug. 2007.

[22] R. N. Govardhan and O. N. Ramesh, "A stroll down Kármán street," *Resonance*, vol. 10, no. 8, pp. 25–37, Aug. 2005.

[23] J. Wang, S. Fu, R. Baarholm, J. Wu, and C. M. Larsen, "Fatigue damage induced by vortex-induced vibrations in oscillatory flow," *Mar. Struct.*, vol. 40, pp. 73–91, Jan. 2015.

[24] E. Egusquiza, C. Valero, X. Huang, E. Jou, A. Guardo, and C. Rodriguez, "Failure investigation of a large pump-turbine runner," *Eng. Fail. Anal.*, vol. 23, pp. 27–34, 2012.

[25] K. J. Lockey, M. Keller, M. Sick, M. H. Staehle, and A. Gehrer. "Flow-induced vibrations at stay vanes: experience on site and CFD simulations of von Kármán vortex shedding," *Int. J. Hydropow. Dams*, no. 5, pp. 102–106, 2006. [Online]. Available: http://fsh.g.andritz.com/c/com2011/00/01/94/19494/1/1/0/738757959/hy-2006-hydro-flow-induced-vibrations-experience-cfd-karman.pdf

[26] Q. Shi, "Abnormal noise and runner cracks caused by von Karman vortex shedding: A case study in Dachaoshan hydroelectric project," in *Proceedings of the 22nd IAHR Symposium on Hydraulic Machinery and Systems*, 2004, paper no. A13-2:1–12.

[27] M. Čudina and J. Prezelj, "Detection of cavitation in operation of kinetic pumps. Use of discrete frequency tone in audible spectra," *Appl. Acoust.*, vol. 70, no. 4, pp. 540–546, 2009.

[28] G. Sridhar and J. Katz, "Effect of entrained bubbles on the structure of vortex rings," *J. Fluid Mech.*, vol. 397, pp. 171–202, Oct. 1999.

[29] J. O. Young and J. W. Holl, "Effects of cavitation on periodic wakes behind symmetric wedges," *J. Basic Eng.*, vol. 88, no. 1, p. 163, 1966.

[30] W. Yang, "Multiobjective optimization design of a pump–turbine impeller based on an inverse design using a combination optimization strategy," *J. Fluids Eng.*, vol. 136, no. 1, p. 14501, Oct. 2013.

[31] V. Hasmatuchi, M. Farhat, S. Roth, F. Botero, and F. Avellan, "Experimental evidence of rotating stall in a pump-turbine at off-design conditions in generating mode," *J. Fluids Eng.*, vol. 133, no. 5, p. 51104, 2011.

[32] C. Widmer, T. Staubli, and N. Ledergerber, "Unstable characteristics and rotating stall in turbine brake operation of pump-turbines," *J. Fluids Eng.*, vol. 133, no. 4, p. 41101, Apr. 2011.

[33] F. Avellan, P. Henry, and I. L. Ryhming, "A new high speed cavitation tunnel," *ASME Winter Annu. Meet.*, vol. 57, pp. 49–60, 1987.

[34] J. Antoni, "Cyclic spectral analysis in practice," *Mech. Syst. Signal Process.*, vol. 21, no. 2, pp. 597–630, 2007.

[35] R. B. Randall, *Vibration-based condition monitoring: Industrial, aerospace and automotive applications*. New York: Wiley, 2011.

[36] H. Nyquist, "Certain topics in telegraph transmission theory," *Proc. IEEE*, vol. 90, no. 2, pp. 280–305, 2002.

[37] C. E. Shannon, "Communication in the presence of noise," *Proc. IEEE*, vol. 86, no. 2, pp. 447–457, Feb. 1998.

[38] J. Antoni, "Cyclic spectral analysis of rolling-element bearing signals: Facts and fictions," *J. Sound Vib.*, vol. 304, no. 3, pp. 497–529, 2007.

[39] J. H. Lienhard, *Synopsis of lift, drag, and vortex frequency data for rigid circular cylinders*. Pullman, Wash.: Technical Extension Service, Washington State University, 1966.

[40] P. D. Welch, "The use of fast Fourier transform for the estimation of power spectra: A method based on time averaging over short, modified periodograms," *IEEE Trans. Audio Electroacoust.*, vol. 15, no. 2, pp. 70–73, Jun. 1967.

[41] M. Farhat, F. Avellan, and F. Pereira, "Pressions instationnaires générées par une poche de cavitation partielle," *Houille blanche*, vol. 47, no. 7–8, pp. 579–585.

[42] X. Escaler, E. Egusquiza, M. Farhat, F. Avellan, and M. Coussirat, "Detection of cavitation in hydraulic turbines," *Mech. Syst. Signal Process.*, vol. 20, no. 4, pp. 983–1007, 2006.

[43] F. Botero, V. Hasmatuchi, S. Roth, and M. Farhat, "Non-intrusive detection of rotating stall in pump-turbines," *Mech. Syst. Signal Process.*, Apr. 2014.

[44] F. Botero, S. Guzman, V. Hasmatuchi, S. Roth, and M. Farhat, "Flow visualization approach for periodically reversed flows," *J. Flow Vis. Image Process.*, vol. 19, no. 4, pp. 309–321, 2012.